

Upgrading the Performance and Stability of Lithium, Manganese-Rich Layered Oxide Cathodes with Combined-Formic Acid and Spinel Coating Treatment

Panawan Vanaphuti^{+[a]}, Luqman Azhari^{+[a]}, Xiaotu Ma,^[a] Yangtao Liu,^[a] Jiahui Hou,^[a] Geoffrey A. Tompsett,^[b] Zhenzhen Yang,^[c] and Yan Wang^{*[a]}

Improving sluggish rate performance and cycling stability of Li, Mn-rich cathode materials (LMR) is of great importance for practical implementation. Here, dual surface modification on LMR particles with formic acid washing and spinel coating improves the electrochemical performance. Dilute formic acid can remove the Li_2CO_3 surface impurities and selectively reduce Ni while significantly increasing specific surface area by $\sim 32\%$, unlocking more electrochemically active surfaces. Spinel coating enhances cycle stability by suppressing detrimental side reactions at electrode-electrolyte interfaces at high voltage. Post-annealing temperature was found to significantly affect the cathode performance. Higher temperature favors diffusion of transition metal (TM)/Li ions of the spinel coating from

surface to the bulk, removing the coating by possible reconstruction into the layered structure and thus degrading the performance. The spinel coating also appears to increase Co^{3+} segregation on the particle surface. Compared to the original material, the optimized sample demonstrates 47% higher capacity retention at 3C and retains 89% of initial capacity after 150 cycles at 0.5C. Besides, the specific energy density of 523 Wh kg^{-1} can be attained after 150 cycles at 0.5C. Moreover, the post-cycling analysis of modified sample verifies a better structural integrity with less particle cracking. Altogether, this study portrays an alternative strategy to overcome the shortcomings of LMR cathode materials.

Introduction

With the constantly growing demand of lithium-ion batteries (LIBs) for electric vehicles, portable electronics, and use in grid storage systems, much research is focused on next-generation cathode materials with higher specific capacities and lower materials costs. Lithium-manganese-rich layered cathode oxides (LMR) are one such material of significant interest, owing to their inherently lower materials cost and alluring energy density ($\sim 900 \text{ Wh kg}^{-1}$) when cycled to high voltages.^[1] The high specific capacity of 250 mAh g^{-1} is attributed to the redox contribution of both TM cations and oxygen (O) anions.^[2] However, several limitations still prevent this cathode from practical applications due to less than desired-capacity degradation, voltage fading, sluggish rate performance, and side reactions with the electrolyte upon subsequent Li intercalation process.^[3,4] Much research has demonstrated that the degra-

tion mechanisms are mainly attributed to the migration of TM and O ions,^[3,5,6] leading to phase transitions from layered to spinel and eventually rock-salt phase.

As solutions to these limitations, various recent studies have aimed to improve the performance of LMR cathode materials by surface modification and doping techniques.^[3,7,8] For instance, acid treatment can regulate and modify the surface composition through delithiation-dissolution processes.^[9] This phenomenon may generate surface Li deficiencies and oxygen vacancies which are believed to alleviate the O release at the surface, and facilitate the reversible anionic redox reaction, allowing better voltage attenuation.^[10-13] For this reason, rate and cycle performance are improved. In fact, the degree of surface Li-deficiency can greatly alter the LMR performance.^[14] Both deionized water and acid treatments have been reported to reduce the Li_2CO_3 surface impurity and increase surface area, which can increase the overall specific capacity by decreasing the interfacial resistance at the electrode/electrolyte interface.^[15,16] McCloskey et al. reported the enhanced electrochemical performance of LMR after H_2SO_4 washing.^[17] By similar means, Aurbach et al. heat treated LMR in the presence of trimesic acid to form co-existing rock-salt and spinel phases to improve the cycling stability.^[18] Note that an initial drop in lithium content was typically observed during short washing steps, accompanied with a large increase in pH of the solution, which is a result of nearly immediate washing away of residual lithium salts that may have remained on the surface during initial calcination of the material.^[19-21] To the best of our knowledge, no work has been reported on using formic acid as a surface treatment method for cathode

[a] P. Vanaphuti,^{+[a]} L. Azhari,^{+[a]} Dr. X. Ma, Y. Liu, J. Hou, Prof. Y. Wang
Department of Mechanical Engineering
Worcester Polytechnic Institute
100 Institute Rd, Worcester, MA 01609
E-mail: yanwang@wpi.edu

[b] Prof. G. A. Tompsett
Department of Chemical Engineering
100 Institute Rd, Worcester, MA 01609

[c] Dr. Z. Yang
Chemical Sciences and Engineering Division
Argonne National Laboratory
9700 S Cass Ave, Lemont, IL 60439

^[+] These authors contributed equally to this work.

Supporting information for this article is available on the WWW under
<https://doi.org/10.1002/batt.202100377>

materials, apart from the Li_2CO_3 recovery in spent LIBs. The main benefits of using formic acid are its relatively low cost and more environmental benign than other acids.

In order to further stabilize the LMR particle surface from Mn dissolution, electrolyte decomposition and HF corrosion, spinel coating with manganese-based compositions is also a promising and effective method as also reported in various recent works.^[12,14,22,23] Specifically, application of a $\text{Li}_4\text{Mn}_5\text{O}_{12}$ coating is chosen as the synergistic strategy after FA treatment to further prolong the cycle life. The coating can be synthesized via a facile method similar to that reported by Guo et al.^[23] Apart from suppressing lattice O loss and Mn dissolution, this spinel coating can also improve the overall rate capability due to the three-dimensional Li interstitial network in the crystal structure.^[22,24]

Here, a combination approach of low-cost formic acid washing and $\text{Li}_4\text{Mn}_5\text{O}_{12}$ coating is employed on LMR cathode particles to enhance the rate and cycle life. Compared to the pristine LMR material (PR), the rate performance of the dual-treated cathode (FA-C-300C) is significantly improved at high charge/discharge rates, where FA-C-300C offers 48% higher reversible capacity at C. From the galvanostatic charge/discharge cycling, the capacity and voltage decay are also alleviated for the treated sample, with a capacity retention of 89% (vs. 71% of PR) and specific energy density retention of 77% (vs. 62% of PR) for the best treated sample after 150 cycles, respectively. Without the spinel coating, samples treated with only formic acid could exhibit even higher rate capabilities across all tested C-rates. However, the undesirable cycling performance is attributed to possible disordered spinel phase formed by Li^+/H^+ exchanges that may trigger undesired reaction with ester-based electrolyte at high voltage and weakened structural integrity. Thus, the overall improved performance of FA-C-300C is due to a combination of the increased electrochemically active surface area of secondary particles without affecting tap density (verified by measurements based on Brunauer, Emmett and Teller (BET) theory and particle size analysis), and protective $\text{Li}_4\text{Mn}_5\text{O}_{12}$ coating to suppress surface-initiated degradation. Interestingly, the post-coating annealing condition greatly affects the LMR performance. Experimentally, 300 °C appears to be the suitable temperature. Increasing the temperature leads to worse performance, attributed to a higher chance of TM diffusion from the coating material into the bulk and rearrangement of the surface composition, which deteriorates the overall performance.

Results and Discussion

Structural and compositional analysis

The particle morphology of treated LMR samples is shown in Figures 1(a–d) and S1. After washing with deionized water or formic acid without agitation, LMR particles do not show significant breakage of the secondary particles. However, this contrasts with those samples washed with agitation, where constant stirring for 24 hours led to significant breakage of the

secondary particles (Figure S2). Compared to PR, the washed samples have small particles on the surface as well as some degree of fractured particles during processing. However, after heat-treatment at 300 °C, the particle surfaces become smoother. In addition, the surface morphology of FA appears to be more porous, with more visible spaces between primary particles. In comparison, the DI surface morphology looks similar to that of PR. The creation of higher surface area in FA is hypothesized to be from acid etching of the secondary particle at grain boundaries, as the formic acid can react with the oxide to form soluble metal formate complexes.^[25,26] This higher surface area remains present even after the coating process, as FA-C-300C also exhibits a similar porous surface morphology. Through BET measurements, the specific surface area is determined to be $4.0 \text{ m}^2 \text{ g}^{-1}$, which is 32% higher than the initial surface area of $2.9 \text{ m}^2 \text{ g}^{-1}$ for PR (Table S1). In fact, this increase in surface area is verified to be due to surface modification rather than breakage of particles, as particle size analysis confirms a nearly identical d₅₀ size of 21.5 μm for both FA-C-300C and PR. Meanwhile, the modified FA-C-300C has only a slightly lower tap density than PR (Table S1), likely due to the mass loss from the acid etching process. The improvement of active surface area, accompanied with only slight decrease in tap density, is desirable for industrial purposes.^[4]

For FA-C samples with $\text{Li}_4\text{Mn}_5\text{O}_{12}$ coating, the annealing temperature significantly affects the particle morphology where higher temperatures result in the smoother and more densely packed primary particles (Figure 1). This is naturally related to the relationship between solid-state ionic diffusion and primary particle growth with temperature.^[27] In addition, Figure S1(e and f) illustrates the SEM-EDS mapping for each metallic element, which has a homogenous distribution along the surface.

ICP-MS data in Table 1 confirms the molar ratio of each metallic element to be closed to the nominal value ($< \pm 5\%$), except for the Li and Mn content. This is theorized to be a result from Li^+/H^+ ion exchange at high pH value for DI and delithiation-dissolution process occurring at low pH solutions for FA where the former results in LiOH formation and negligible TM dissolution. For the latter acid-based reaction, both Li^+ and TM migrate into the solution through oxide etching as well as Li^+/H^+ ion exchange.^[9] Due to the low concentration of the formic acid used in this work, no significant difference in TM dissolution is observed for formic acid treated samples and it appears that Li ions preferentially leaches out of the cathode materials faster than TM ions

Table 1. Molar ratio of each metallic elements from ICP-MS analysis.

Sample	Molar ratio			
	Li	Mn	Ni	Co
Target Ratio	1.200	0.540	0.130	0.130
PR	1.182	0.548	0.136	0.134
DI	1.152	0.576	0.133	0.139
FA	1.138	0.589	0.132	0.141
LMR-FA-C-300C	1.103	0.622	0.132	0.143
LMR-FA-C-550C	1.094	0.629	0.133	0.144
LMR-FA-C-750C	1.088	0.632	0.134	0.146

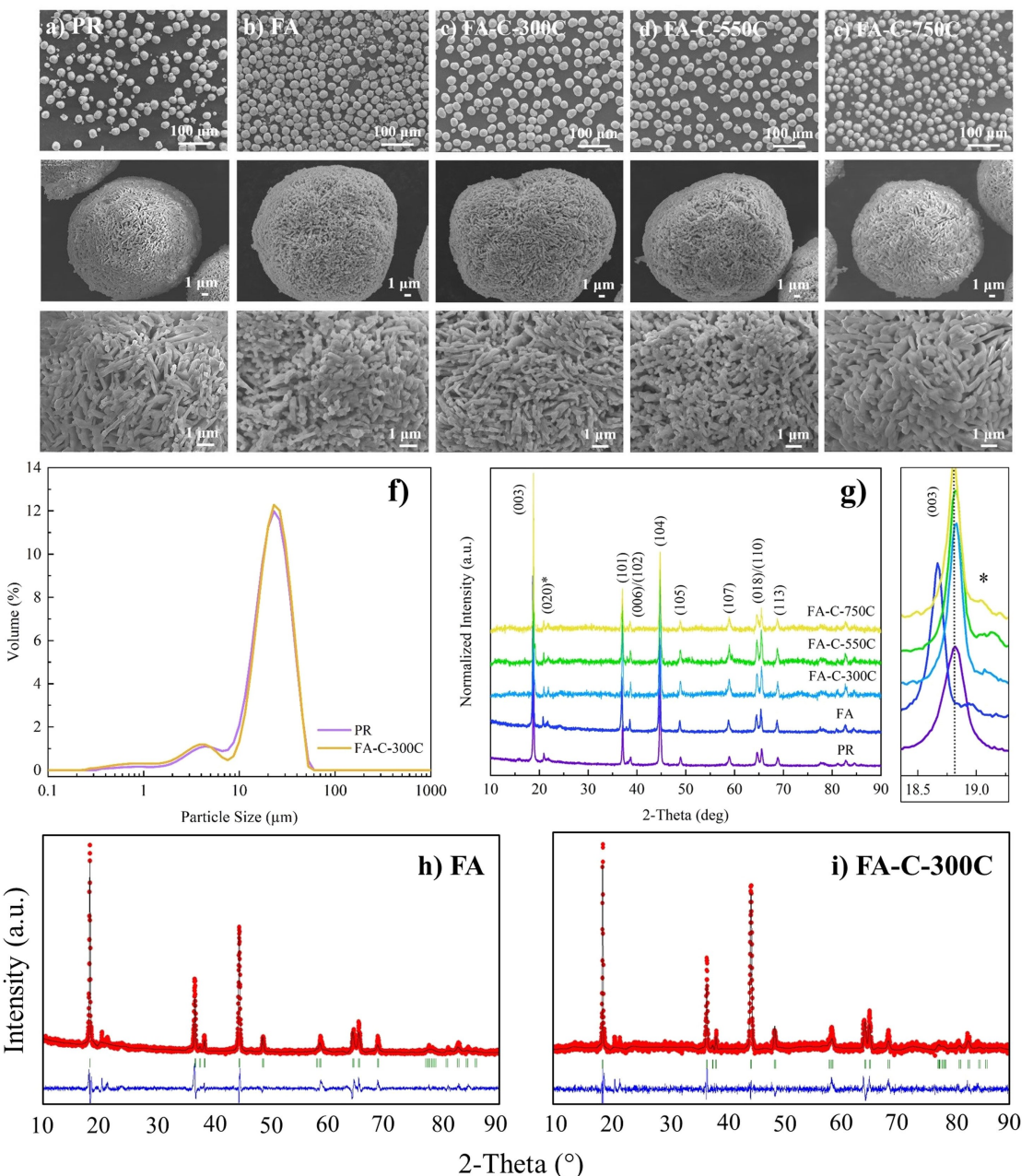


Figure 1. Morphological and structural analysis of PR and treated samples; SEM images of a) PR, b) FA, c) FA-C-300C, d) FA-C-550C, e) FA-C-750C, f) Particle size distribution for PR and FA-C-300C sample, g) XRD patterns with $\text{Cu } K_{\alpha}$ target where the asterisk (*) indicates the spinel phase signal from (111) plane, and refinement profile for h) FA and i) FA-C-300C.

(Table 1). Likewise, about 10% of Mn ratio is increased in the spinel coated samples, resulting from the Mn-rich spinel coating on the surface of LMR.^[13,23]

Structural parameters determined from XRD patterns ($\text{Cu } K_{\alpha}$ target) are shown in Figures 1(g) and S3 with the corresponding refinement profiles in Figures 1(h and i) and S4. All peaks are well-matched with layered $\alpha\text{-NaFeO}_2$ structure (R-3 m) except for a small superlattice signal at $\sim 21^\circ$. This peak refers to the LiMn_6 cation ordering of monoclinic structure (C2/m).^[28] Interestingly, both DI and FA treatment can modulate the superlattice ordering as the signal is distinct from the PR. Note that the shoulder peak around $\sim 19^\circ\text{--}20^\circ$ reveals the character-

istics of $\text{Li}_4\text{Mn}_5\text{O}_{12}$ spinel phase ((111) plane) presented in the treated samples.^[14,23] It is noteworthy that the spinel peak intensity shifts to the left and increases as the annealing temperature increases suggesting the decomposition of spinel phase to layered phase from the rearrangement of lattice ordering induced at high temperature. Table 2 displays the refined values for all samples. For DI and FA, the degree of cation mixing is increased, which highlights the contribution of cation disorder in the lattice. The addition of a spinel coating in the case of FA-C samples creates an even more distorted structure (cation mixing) and volume shrinkage than the bare FA. This is ascribed to the cation-disordered spinel layer

Table 2. Refined structural parameters from FullProf Suite software with ICSD No. 04-013-5383 as the standard pattern for the pristine state.

Sample	a/b-axes [Å]	c-axis [Å]	Volume [Å ³]	Ni in Li Layer [%]	Occ. [O]	X ²
PR	2.85495	14.29088	100.875	4.76	1.000	5.34
DI	2.85515	14.30527	100.992	18.1	0.916	3.89
FA	2.85496	14.30531	100.979	16.5	0.955	3.83
FA-C-300C	2.85033	14.20885	99.973	6.31	0.976	7.54
FA-C-550C	2.85272	14.22848	100.279	5.74	0.827	7.09
FA-C-750C	2.85662	14.30722	101.109	4.08	0.794	5.99

formation that decreases the overall layered configuration. Another significant characteristic is that the O occupancy is lowered after the treatment, from 1.000 to 0.976, indicating the possibility of generated O vacancies. Since FA-C-300C has a contraction in the c lattice parameter, it can be expected that the high specific capacity does not contribute from the improved Li diffusivity from the Li slab. It is probably related to the increase active surface area and spinel coating, where the spinel structure allows for multiple Li diffusion pathways due to its three-dimensional interstitial network, thus resulting in the improved rate performance.

Degree of spinel surface formation

The presence of spinel coating is examined using Raman microscopy, which is sensitive to the surface structure by probing molecular vibrations. This technique is structure and atom dependent. Prior work has demonstrated the ability to distinguish between various transition metal-oxygen bonds, in

particular the TM–O bonding in hexagonal R-3 m structures and spinel Fd-3 m structures.^[25,26] Figures 2(a) and S5 show Raman spectra for each sample. The major bands of monoclinic Li_2MnO_3 -like phase are observed near 427 and 562 cm⁻¹. For the layered LiTMO_2 phase, bands are observed at 490 cm⁻¹ (in-plane O–TM–O bending mode) and 595 cm⁻¹ (out-of-plane TM–O stretching mode).^[29,30] Note that the characteristic band for the spinel-like phase is located at a higher Raman shift of ~651 cm⁻¹, which is due to the shorter and higher energy of TM–O bonds in the spinel structure.^[31] Even prior to the application of spinel coating, the spinel-like phase is already presented in DI and FA samples, which indicates that even only washing step can modify the particle surface to a certain level depending on the reaction with different pH solution (Li^+/H^+ exchange).^[9] By comparing the integrated areas of the main peaks between layered and spinel phase (651/595 cm⁻¹), a Raman band intensity ratio can be determined, which can be computed from the ratio of the layered and spinel phases presented near the surface regions (Figures 2c–e and S6). As expected, a higher degree of spinel formation exists in FA and

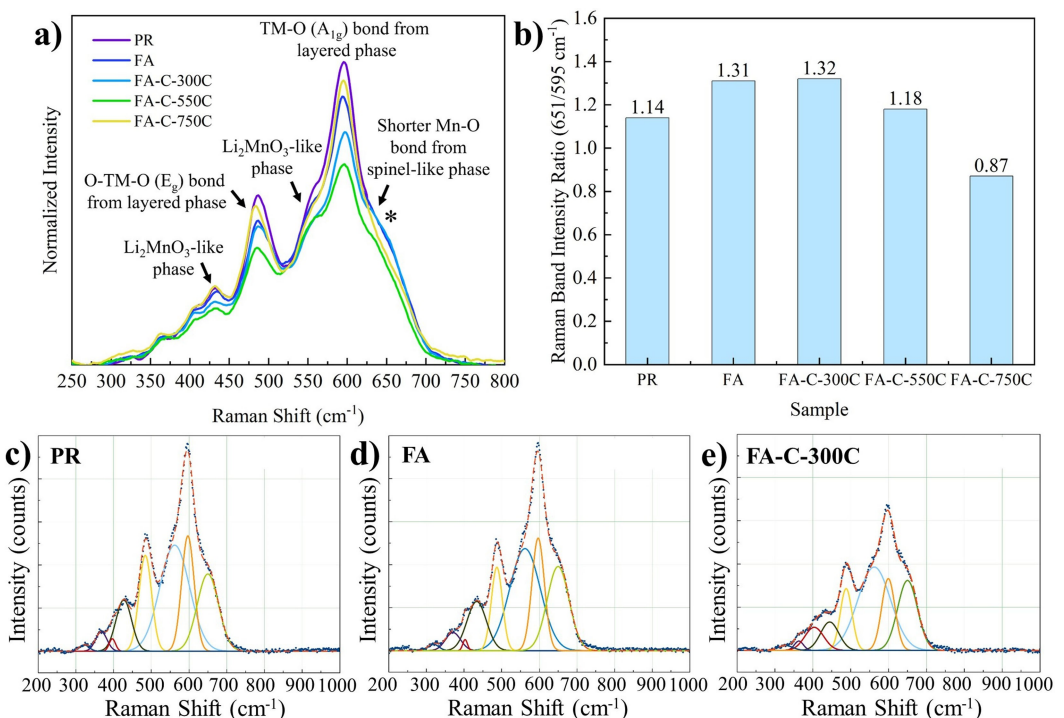


Figure 2. Particle surface analysis with Raman microscope; a) resulted Raman spectra for each sample, b) Raman band intensity ratio (651/595 cm⁻¹) between spinel to layered phase and the fitted peak profile for c) PR, d) FA and e) FA-C-300C.

FA-C-300C (Figure 2b) compared to PR. In addition, with the added $\text{Li}_4\text{Mn}_5\text{O}_{12}$ in FA-C-300C, the level of spinel formation increases than that of FA, which confirms the treatment can generate artificial spinel coating on the particle surface. Meanwhile, increasing the temperature is found to decrease the level of spinel phase.

Electrochemical performance

Figures 3(a) and S7(a) compare the rate performance for each sample at various charge/discharge rates from 0.05C–3C. In contrast to PR, all treated samples can provide some level of improvement to the reversible specific capacity for the rate tests. The best rate performances were observed for FA and FA-C-550C owing to the increased surface area and excess Li deficiencies that induced disordered spinel layer. However, too much structural disordering can hasten the capacity degradation over extended cycling. This is thought to be the reason that FA and FA-C-550C retains only 67% and 76% of their

initial capacity after 150 cycles at 0.5C, respectively. In addition, the voltage profile of the first cycle (Figure 3b) shows the optimized oxygen redox plateau (~ 4.5 V) with first columbic efficiency of 85% for FA-C-300C (73% of PR and 76% of FA). While DI exhibited modest improvement in rate performance (171 vs. 150 mAh g^{-1} at 1C, Figure S7), FA samples were selected for further spinel coating processes due to the attractive specific capacity. It is worth mentioning that both DI and FA samples contain spinel structure according to the XRD and Raman results. However, the spinel phase generated by artificial Li coating is better than Li^+/H^+ exchange process when considered the electrochemical performance. Besides, the capacity retention for FA-C-300C at 3C is 48% higher than that of PR (101 vs. 62 mAh g^{-1}). The higher specific capacity of FA-C-300C compared to PR derives from the spinel phase in combination with the decrease of Li_2CO_3 resistive surface that can provide more electrochemically active surfaces and shorter Li diffusion pathways between the electrode-electrolyte interface. Note that the slight difference in specific capacity during the initial cycles (~ 5 cycles) in Figure 3f compared to Fig-

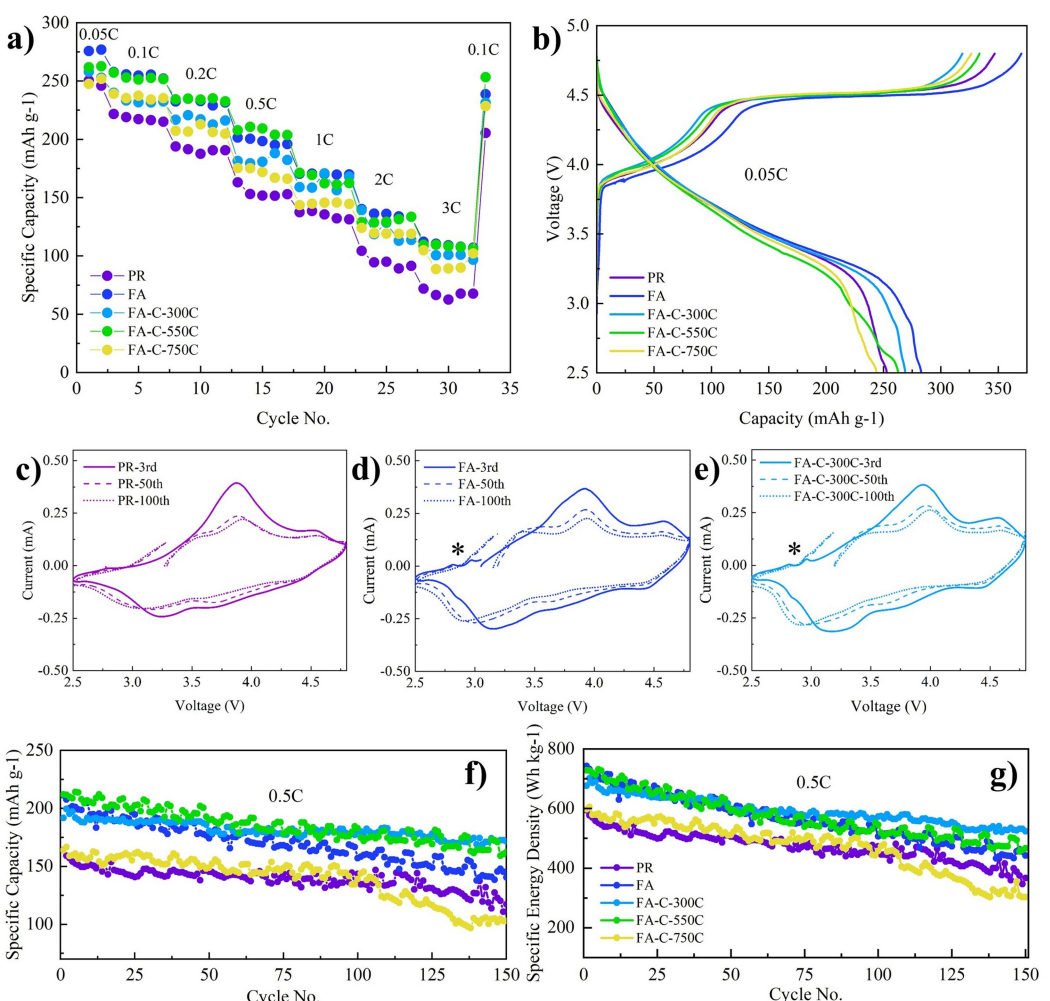


Figure 3. Electrochemical performance for each sample; a) rate, b) voltage profile of the first cycle, c–e) CV curves at the scan rate of 0.1 mV s^{-1} where the asterisk (*) indicates the characteristic signal of spinel-like phase for c) PR, d) FA and e) FA-C-300C, f) cycle performance, and g) specific energy density at 0.5C for 150 cycles. All testing is performed at room temperature between the voltage range of 2.5–4.8 V ($1\text{C} = 250 \text{ mAh g}^{-1}$).

ure 3(a) is attributed to the sluggish activation kinetics of Li_2MnO_3 monoclinic phase in Li, Mn-rich materials.^[32,33] Hence, the most optimized performance with good rate capacity and cycle life duration is FA-C-300C (Figure 3f and g) with capacity and specific energy density retention of 89% (vs. 72% of PR) and 77% (vs. 62% of PR) after 150 cycles at 0.5C, respectively. As opposed to FA-C-300C, the cycle performance of FA-C-550C and FA-C-750C are exacerbated due to the nonideal annealing temperature which likely deteriorates the spinel coating without properly forming the complete layered phase.

To examine the degree of oxygen participation, CV profiles are evaluated (Figures 3c–e, S7b and S8) where the signal around 4.6 V is attributed to the $\text{O}^{2-}/\text{O}^{n-}$ ($n < 2$)/ O_2 oxidation peak. The relative intensity of this peak can be correlated to the quantity of O contribution in the redox reaction during Li intercalation process. The major signal at ~ 4.0 V corresponds to the overlap of oxidation reaction for $\text{Ni}^{2+/4+}$ and $\text{Co}^{3+/4+}$. During the discharge process, the reduction reaction occurs from $\text{Co}^{4+/3+}$ (4.4 V), $\text{Ni}^{4+/2+}$ (3.8 V), and then $\text{Mn}^{4+/3+}$ (3.25 V) in sequence from high to low potential.^[34,35] As shown in Figures 3(c–e) and S8, more reversible O redox happens in FA, FA-C-300C and FA-C-550C compared to other samples. Besides, during Li insertion (discharge), the TM reduction is more distinct for these samples akin to PR and FA-C-750C resulting from the better Li diffusion pathway on the surface. Altogether, this corresponds to the observed high specific capacity. The direct evidence that spinel coating exists in the treated samples and participates in the redox reaction can be seen from the small signal around 2.8 V, representing the Mn redox reaction of spinel phase where the Li ions are inserted in 16c octahedral sites during the intercalation process.^[36,37] This finding is consistent with XRD and Raman data. In contrast, such redox peaks are not obvious in PR and FA-C-750C. Hence, by increasing the annealing temperature to 750 °C, the structure can partially be reverted to a well-ordered layered structure similar to that of PR. However, the specific capacity is also reduced.

Impact of the surface treatment on the oxidation state of transition metals

The surface composition and valance state of the TM ions are examined with high resolution XPS for the selected samples including FA, FA-C-300C, and FA-C-750C. The resulting spectra are shown in Figures 4 and S9. Note that the XPS data of PR have been reported in our previous work.^[38] For Mn 2p, the main signals are around 642 eV (Mn 2p3/2) and 654 eV (Mn 2p1/2), while the Mn^{3+} peaks are located at 642 eV and 653.5 eV. For Mn^{4+} state, the peaks are slightly higher at around 643 eV and 655 eV. For Ni^{2+} state, the peaks include 854.5 eV (2p3/2) and 872.1 eV (2p1/2) with co-existing Ni^{3+} signals at 856 eV (2p3/2) and 874 eV (2p1/2). Likewise, the peak positions at 781 eV (2p3/2) and 796.7 eV (2p1/2) can be correlated to Co^{2+} whereas peaks at 780 eV (2p3/2) and 795 eV (2p1/2) represent the Co^{3+} state.^[39] Overall, the peak positions

of treated samples do not show a dominant shift from the pristine state.

Post-cycling analysis

To evaluate the structural stability between PR and treated samples, post-mortem analysis of cycled electrodes after 150 cycles at 0.5C was analyzed, as shown in Figure 5. Note that prior to the ex-situ testing, all electrodes were thoroughly rinsed with dimethyl carbonate (DMC) to remove the residual electrolyte and left in the glovebox until dry. The SEM image of FA-C-300C shows the least particle breakage induced by the lattice strain during the Li intercalation process, with the order of fracture severity from low to high is FA-C-300C < FA < FA-C-550C ~ PR < FA-C-750C (Figure 5a–e). Hence, increasing the resintering temperature can greatly degrade the cathode performance due to the Li/Mn ionic diffusion of spinel coating from the surface to the bulk. This can deteriorate the ability of the coating to improve cycle retention from electrolyte decomposition and HF corrosion. In Figure 5f and Table S3, the EIS data further reveals the superior performance of FA-C-300C with lowest R_{SEI} value (19% lower than PR).

XRD refinement of post-cycled electrodes are also determined as shown in Figure 5g–i and Figure S10, with the corresponding refined parameters provided in Table S4. Compared to the pristine state, all samples show some degree of lattice expansion except for PR and FA-C-750C, which exhibits lattice contraction after cycling. The contraction of c-axis may relate to lattice strain triggered by the TM migration and irreversible O_2 release. Besides, the percent of Ni in Li layer after cycle is in the order of FA-C-300C < FA < FA-C-550C < FA-C-750C < PR. Therefore, this further confirms the ability of the synergistic strategy to maintain the good structural integrity after cycling. On the contrary, PR and FA-C-750C has a very high cation ordering at the pristine state but undergoes significant structural changes after cycling.

Conclusion

This work provides a synergistic surface modification strategy to improve the structural stability of LMR through a facile formic acid washing and spinel coating. In comparison to PR, the electrochemical performance of FA-C-300C is significantly enhanced in which the capacity retention at 3C is improved by 48%. Cycle stability is also improved with FA-C-300C retaining 89% of its initial capacity after 150 cycles at 0.5C and a specific energy retention of 523 Wh kg⁻¹. From PSA and BET data, a dilute concentration of FA increases the surface area via gentle etching with negligible breakage of the cathode particles. Meanwhile, the application of a $\text{Li}_4\text{Mn}_5\text{O}_{12}$ coating can improve the structural stability at the electrode-electrolyte interface during high-voltage cycling. The annealing temperature of the spinel coating has great influence on the particle surface morphology and composition. By increasing the temperature, the ionic diffusion (TM/Li) of coating material from the surface

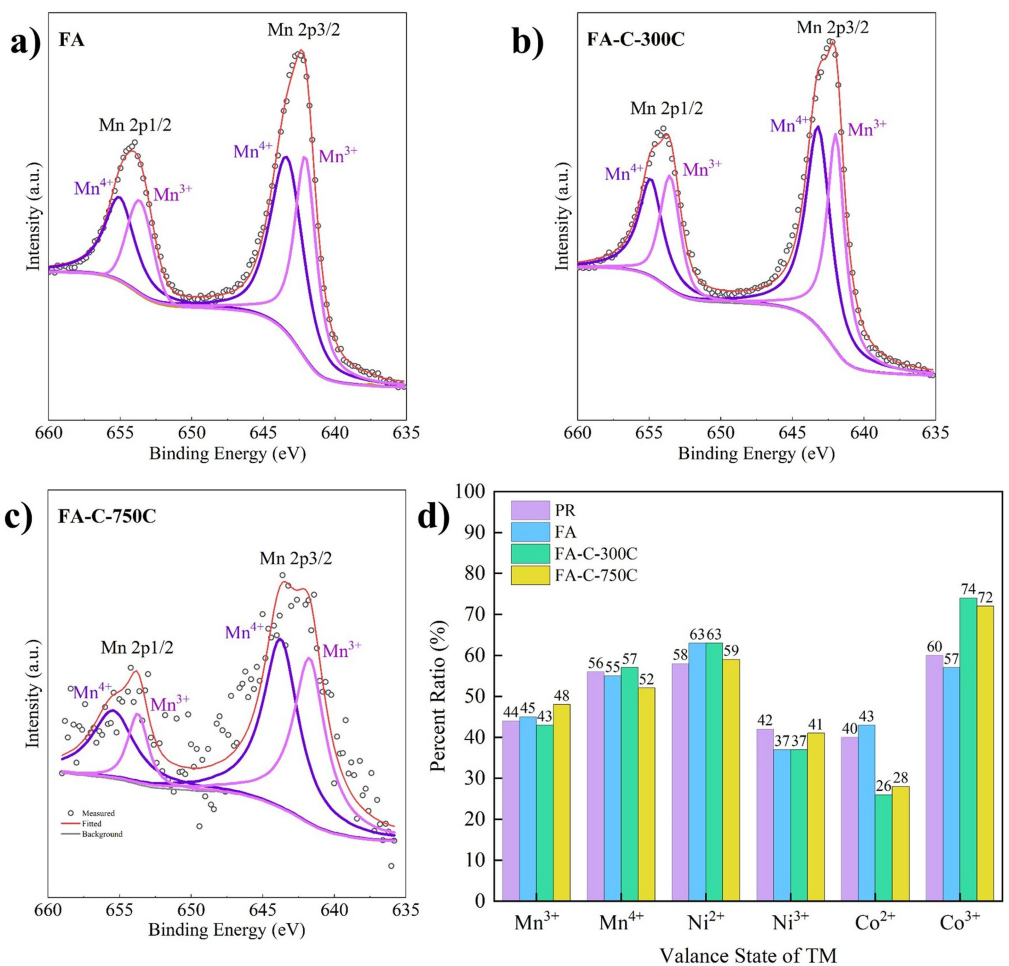


Figure 4. Surface compositional analysis via high resolution XPS spectra of fitted Mn 2p spectra at pristine state for a) FA, b) FA-C-300C, c) FA-C-750C, and d) the percent ratio of different TM valance states computed from 2p3/2 peak area.

to the bulk is favored. This leads to the failure of the coating layer to provide a positive effect on the electrochemical performance. In addition, spinel coating can increase the amount of Co³⁺ segregation on the particle surface according to XPS data. The post-mortem analysis of the cycled electrodes verifies that the FA-C-300C has more structural integrity compared to other samples. Hence, this study displays an alternative and facile approach in enhancing the LMR performance with dual surface modification, which can also be directly utilized in other high-energy cathode materials.

Experimental Section

Synthesis of LMR layered oxides and surface treatment conditions: The LMR cathode is synthesized via hydroxide co-precipitation and solid-state reaction as reported in our previous work.^[40] The LMR cathode particles were then washed with distilled water at 60°C, or 0.05 M formic acid (Sigma-Aldrich) at room temperature for 24 h at a ratio of 1 g/1 mL solution. The powders were submerged without agitation for the majority of the washing step to prevent particle breakage whereas the time of 24 h was fixed for all conditions to make sure all LMR particles were thoroughly washed in the

specified solutions. Note that 60°C was used for distilled water to favor the washing process since the reaction will be much slower at room temperature.^[13] Meanwhile, the parafilm cannot withstand high temperature and open system can cause evaporation of distilled water leading to variation in the concentration. The collected powders were rinsed with deionized water under vacuum filtration and dried at 70°C. Then, the powders were annealed at 300°C under air atmosphere for 10 h where the distilled water and formic acid treatment were named as DI and FA, respectively. Due to the morphology and performance, the FA sample was chosen to further be treated with Li₄Mn₅O₁₂ coating via the KMnO₄ oxidation method.^[23] Precisely, 0.0167 M KMnO₄ (Sigma-Aldrich) solution was prepared in deionized water, then FA cathode powders (before 300°C annealing) and KMnO₄ solution were mixed on a roller table for two hours at room temperature with a solids to solution ratio of 0.5 g/15 mL. After rinsing and filtering of the coated powders to remove excess KMnO₄, the resulting powders were annealed at various temperatures under air atmosphere to determine the optimized condition. The heating and cooling rate was kept constant at 5°Cmin⁻¹. The as-prepared powders annealed at 300°C, 550°C and 750°C for 10 h were named as FA-C-300C, FA-C-550C and FA-C-750C, respectively. Note that 300°C was chosen for low range temperature as lower than 300°C would not cause significant effect on diffusivity of TM metals/O ordering. In contrast, higher than 750°C would be closed to the temperature for complete formation of the layered structure.

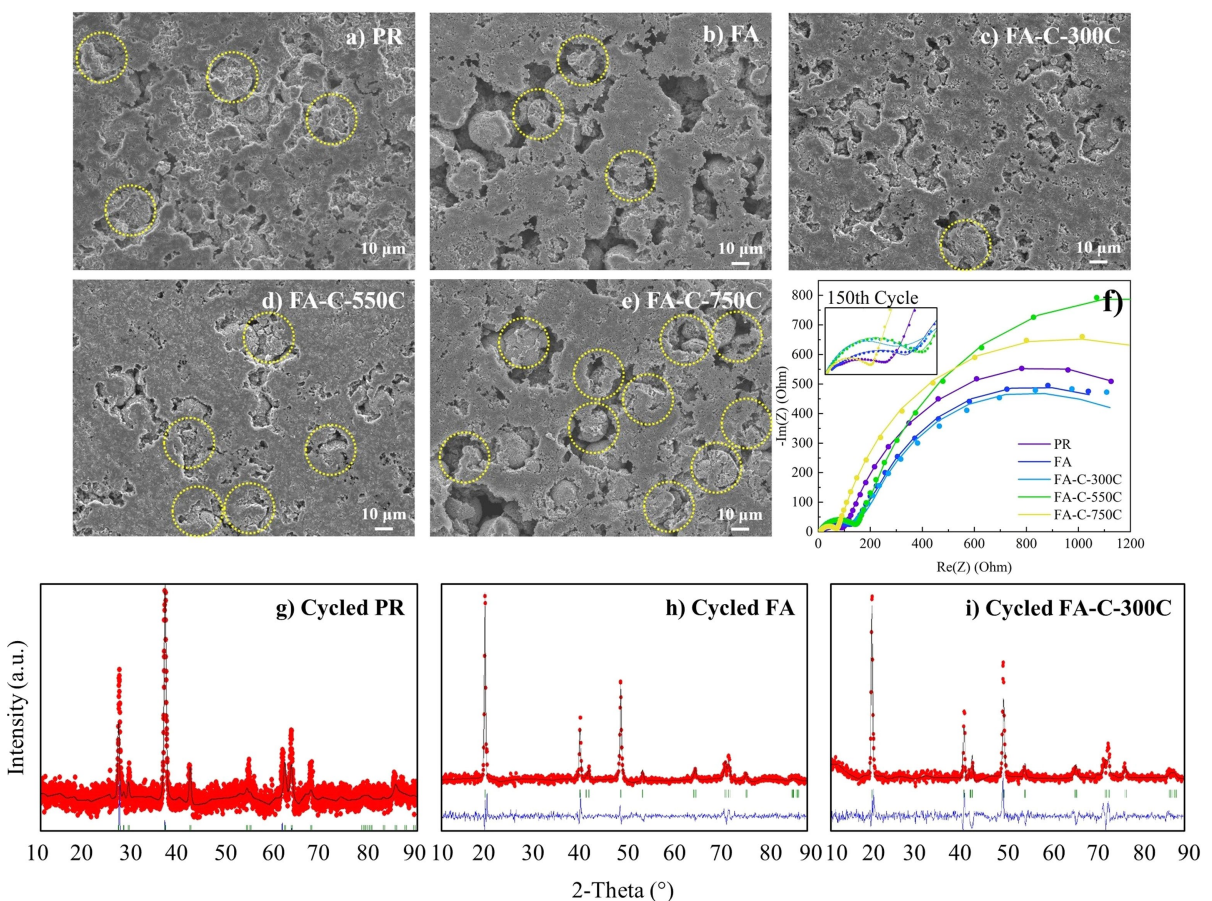


Figure 5. Post-mortem analysis after 150 cycles; SEM images of cycled electrodes where yellow circles indicate the particle fractures for a) PR, b) FA, c) FA-C-300C, d) FA-C-550C, and e) FA-C-750C. The EIS spectra for all samples f) where the inset shows the closed-up view. The fitted data is shown in Table S3. Rietveld refinement profile of g) cycled PR, h) cycled FA and i) cycled FA-C-300C using Cu K_{α} target and ICSD No. 04-013-5383 as the standard pattern. The refined parameters are shown in Table S4.

Materials characterization: Structural analyses were examined using scanning electron microscopy (SEM) coupled with energy-dispersive X-ray spectroscopy (SEM-EDS; JEOL JSM 7000F) and X-ray diffraction (XRD; PANalytical Empyrean, Cu K_{α} target, $\lambda = 1.54 \text{ \AA}$). FullProf Suite software was employed to compute the crystal lattice parameters via Rietveld Refinement method with $\text{LiMn}_{0.5}\text{Ni}_{0.5}\text{O}_2$ (ICSD No. 04-013-5383) as the reference pattern. The molar ratios and chemical compositions of the as-prepared cathodes were obtained via inductively coupled plasma mass spectrometry (ICP-MS). The ICP-MS samples were prepared by dissolving the LMR powders in the aqua regia solution, which consists of a mixture between nitric acid and hydrochloric acid in the 1:3 ratio. Detailed surface analyses were obtained using X-ray photoelectron spectroscopy (XPS; PHI 5000 VersaProbe II) and Raman microscopy (Horiba Xplora). The XPS conditions were the same as that reported elsewhere^[38] and the corresponding XPS data were fitted using XPSpeak41 software. The obtained spectra were calibrated in reference to the C 1s peak position (284.8 eV). For Raman spectroscopy, the laser light ($\lambda = 532 \text{ nm}$) was used with 1800 grating, 10% attenuated power, and an objective lens of 100x. A gold coated silicon wafer was used to support the powder samples. MagicPlot software was employed to do the baseline and peak fitting of the corresponding Raman spectra. The acquisition and accumulation time was set to 5s and 30s, respectively. Specific surface area and particle size distribution of before and after treatment samples (PR and FA-C-300C) were determined using BET

surface area measurements (Micromeritics ASAP 2020) and particle size analyzer (PSA; Mastersizer 2000).

Electrochemical testing: All 2032-coin cells were built in Argon-filled glovebox composing of the different LMR samples, Li metal anode, trilayer polypropylene-polyethylene-polypropylene separator, and 1.0 M LiPF_6 in EC/EMC (3:7 weight ratio) liquid electrolyte (Gotion). For the positive electrode, the composition was 80 wt % active material, 10 wt % super C65 carbon black (MSE Supplies LLC), and 10 wt % polyvinylidene fluoride (PVDF). A slurry was prepared using NMP solvent, and subsequently casted on Al foil using a doctor blade thickness of 150 μm . The active material loading was maintained at $3.0 \pm 0.5 \text{ mg cm}^{-2}$. All the electrochemical testing was performed at room temperature using a Land Battery Testing System (LAND CT2001 A) at voltage range of 2.5–4.8 V vs. Li/Li⁺ ($1\text{C} = 250 \text{ mA h g}^{-1}$). Cyclic voltammetry (CV) and electrochemical impedance spectroscopy (EIS) data were collected via a Bio-Logic SAS VMP3 potentiostat. For EIS, the applied frequency range and amplitude were 10 mHz–100 kHz and 10 mV, respectively. The CV was tested at 0.1 mV s^{-1} for the 3rd, 50th and 100th cycle after completed two formation cycles at constant current of 0.05C and subsequent cycles at constant current of 0.5C.

Author Contributions

P. Vanaphuti and L. Azhari contributed equally to this work. All authors have given approval to the final version of the manuscript.

Acknowledgements

The authors genuinely acknowledge the Department of Chemistry, Chulalongkorn University in collaboration with Bangkok Bank Public Co., Ltd (Thailand) for a graduate fellowship awarded to P. Vanaphuti. XPS analysis was conducted at Post Test Facility of Argonne National Laboratory, operated for DOE Office of Science by UChicago Argonne, LLC, under the Contract No. DE-AC02-06CH11357. We greatly appreciate Professor Michael T. Timko from Department of Chemical Engineering at WPI for the use of the Raman microscopy.

Conflict of Interest

The authors declare that they have no known competing financial interests that could have appeared to influence the work reported in this paper.

Data Availability Statement

Research data are not shared.

Keywords: formic acid • high-energy cathodes • Li-rich layered oxides • spinel coating • surface treatment

- [1] H. Pan, S. Zhang, J. Chen, M. Gao, Y. Liu, T. Zhu, Y. Jiang, *Mol. Syst. Des. Eng.* **2018**, *3*, 748–803.
- [2] A. R. Armstrong, M. Holzapfel, P. Novák, C. S. Johnson, S. H. Kang, M. M. Thackeray, P. G. Bruce, *J. Am. Chem. Soc.* **2006**, *128*, 8694–8698.
- [3] G. Assat, J. M. Tarascon, *Nat. Energy* **2018**, *3*, 373–386.
- [4] J. Zheng, S. Myeong, W. Cho, P. Yan, J. Xiao, C. Wang, J. Cho, J. G. Zhang, *Adv. Energy Mater.* **2017**, *7*, DOI 10.1002/aenm.201601284.
- [5] P. M. Csernica, S. S. Kalirai, W. E. Gent, K. Lim, Y. S. Yu, Y. Liu, S. J. Ahn, E. Kaeli, X. Xu, K. H. Stone, A. F. Marshall, R. Sinclair, D. A. Shapiro, M. F. Toney, W. C. Chueh, *Nat. Energy* **2021**, *6*, 642–652.
- [6] J. R. Croy, K. G. Gallagher, M. Balasubramanian, B. R. Long, M. M. Thackeray, *J. Electrochem. Soc.* **2014**, *161*, 318–325.
- [7] S. Hy, H. Liu, M. Zhang, D. Qian, B. J. Hwang, Y. S. Meng, *Energy Environ. Sci.* **2016**, *9*, 1931–1954.
- [8] K. Zhang, B. Li, Y. Zuo, J. Song, H. Shang, F. Ning, D. Xia, *Electrochem. Energy Rev.* **2019**, *2*, 606–623.
- [9] I. Hamam, N. Zhang, A. Liu, M. B. Johnson, J. R. Dahn, *J. Electrochem. Soc.* **2020**, *167*, 130521.
- [10] Z. Yang, J. Zhong, J. Feng, J. Li, F. Kang, *Chem. Eng. J.* **2021**, *427*, 130723.
- [11] T. Nakamura, K. Ohta, X. Hou, Y. Kimura, K. Tsuruta, Y. Tamenori, R. Aso, H. Yoshida, K. Amezawa, *J. Mater. Chem. A* **2021**, *9*, 3657–3667.

- [12] S. Li, H. Zhang, H. Li, S. Zhang, B. Zhu, S. Wang, J. Zheng, F. Liu, Z. Zhang, Y. Lai, *ACS Appl. Mater. Interfaces* **2021**, *13*, 39480–39490.
- [13] M.-J. Wang, A.-F. Shao, F.-D. Yu, G. Sun, D.-M. Gu, Z.-B. Wang, *ACS Sustainable Chem. Eng.* **2019**, *7*, 12825–12837.
- [14] Y. Liu, Y. Liu, Y. Liu, H. Zhuo, H. Zhuo, H. Zhuo, Y. Yin, Y. Yin, S. Lu, S. Lu, Z. Wang, Z. Wang, W. Zhuang, W. Zhuang, W. Zhuang, *ACS Appl. Mater. Interfaces* **2020**, *12*, 27226–27240.
- [15] M. Wood, J. Li, R. E. Ruther, Z. Du, E. C. Self, H. M. Meyer, C. Daniel, I. Belharouak, D. L. Wood, *Energy Storage Mater.* **2020**, *24*, 188–197.
- [16] S. S. Zhang, L. Ma, *J. Electrochem. Soc.* **2021**, *168*, 080512.
- [17] S. Ramakrishnan, B. Park, J. Wu, W. Yang, B. D. McCloskey, *J. Am. Chem. Soc.* **2020**, *142*, 8522–8531.
- [18] S. Maiti, H. Sclar, Rosy, J. Grinblat, M. Talianker, L. Burstein, M. Noked, B. Markovsky, D. Aurbach, *ACS Appl. Mater. Interfaces* **2020**, *12*, 32698–32711.
- [19] C. X. Zhou, P. B. Wang, B. Zhang, L. B. Tang, H. Tong, Z. J. He, J. C. Zheng, *ACS Appl. Mater. Interfaces* **2019**, *11*, 11518–11526.
- [20] J. H. Park, B. Choi, Y. S. Kang, S. Y. Park, D. J. Yun, I. Park, J. H. Shim, J. H. Park, H. N. Han, K. Park, *Energy Technol.* **2018**, *6*, 1361–1369.
- [21] S. E. Renfrew, B. D. McCloskey, *J. Am. Chem. Soc.* **2017**, *139*, 17853–17860.
- [22] Y. Lee, T. H. Kim, Y. K. Kwon, J. Shin, E. A. Cho, *ACS Sustainable Chem. Eng.* **2020**, *8*, 8037–8048.
- [23] X. D. Zhang, J. L. Shi, J. Y. Liang, Y. X. Yin, J. N. Zhang, X. Q. Yu, Y. G. Guo, *Adv. Mater.* **2018**, *30*, 1–8.
- [24] W. Zhu, Z. Tai, C. Shu, S. Chong, S. Guo, L. Ji, Y. Chen, Y. Liu, *J. Mater. Chem. A* **2020**, *8*, 7991–8001.
- [25] B. W. Krupay, R. A. Ross, *J. Catal.* **1975**, *39*, 369–374.
- [26] J. P. Durand, S. D. Senanayake, S. L. Suib, D. R. Mullins, *J. Phys. Chem. C* **2010**, *114*, 20000–20006.
- [27] V. Pimenta, M. Sathiya, D. Batuk, A. M. Abakumov, D. Giaume, S. Cassaignon, D. Larcher, J. M. Tarascon, *Chem. Mater.* **2017**, *29*, 9923–9936.
- [28] C. R. Fell, D. Qian, K. J. Carroll, M. Chi, J. L. Jones, Y. S. Meng, *Chem. Mater.* **2013**, *25*, 1621–1629.
- [29] C. Y. Li, Z. Q. Tian, Y. Yu, C. Wang, Y. Zhang, S. Y. Zheng, J. F. Li, F. Maglia, R. Jung, Y. Shao-Horn, *J. Phys. Chem. C* **2020**, *124*, 4024–4031.
- [30] J. X. Huang, B. Li, B. Liu, B. J. Liu, J. B. Zhao, B. Ren, *J. Power Sources* **2016**, *310*, 85–90.
- [31] C. V. Ramana, M. Massot, C. M. Julien, *Surf. Interface Anal.* **2005**, *37*, 412–416.
- [32] P. K. Nayak, J. Grinblat, E. Levi, M. Levi, B. Markovsky, D. Aurbach, *Phys. Chem. Chem. Phys.* **2017**, *19*, 6142–6152.
- [33] X. Feng, Y. Gao, L. Ben, Z. Yang, Z. Wang, L. Chen, *J. Power Sources* **2016**, *317*, 74–80.
- [34] H. Zheng, Z. Hu, P. Liu, W. Xu, Q. Xie, W. He, Q. Luo, L. Wang, D. Gu, B. Qu, Z. Z. Zhu, D. L. Peng, *Energy Storage Mater.* **2020**, *25*, 76–85.
- [35] X. Ji, Y. Xu, H. Feng, P. Wang, Y. Zhou, J. Song, Q. Xia, Q. Tan, *ACS Appl. Mater. Interfaces* **2021**, *13*, 47659–47670.
- [36] F. Da Yu, L. F. Que, Z. B. Wang, Y. Zhang, Y. Xue, B. S. Liu, D. M. Gu, *J. Mater. Chem. A* **2016**, *4*, 18416–18425.
- [37] J. Han, H. Zheng, Z. Hu, X. Luo, Y. Ma, Q. Xie, D. L. Peng, G. Yue, *Electrochim. Acta* **2019**, *299*, 844–852.
- [38] P. Vanaphuti, Y. Liu, X. Ma, J. Fu, Y. Lin, J. Wen, Z. Yang, Y. Wang, *ACS Appl. Mater. Interfaces* **2021**, *13*, 22597–22607.
- [39] N. Andreu, D. Flahaut, R. Dedryvère, M. Minvielle, H. Martinez, D. Gonbeau, *ACS Appl. Mater. Interfaces* **2015**, *7*, 6629–6636.
- [40] P. Vanaphuti, J. Chen, J. Cao, K. Bigham, B. Chen, L. Yang, H. Chen, Y. Wang, *ACS Appl. Mater. Interfaces* **2019**, *11*, 37842–37849.

Manuscript received: December 3, 2021
Revised manuscript received: December 18, 2021
Accepted manuscript online: January 11, 2022
Version of record online: January 19, 2022